POLITECNICO
MILANO 1863

DIPARTIMENTO DI MECCANICA

mecc

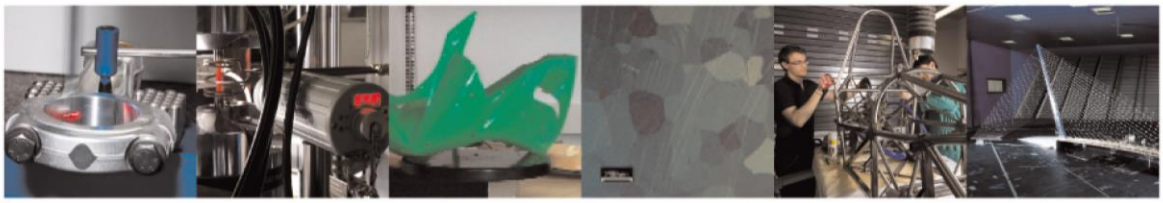

Selective laser melting of pure Zn with high density for biodegradable implant manufacturing

Demir, Ali Gökhan; MONGUZZI, LORENZO; Previtali, Barbara

This is a post-peer-review, pre-copyedit version of an article published in ADDITIVE MANUFACTURING. The final authenticated version is available online at: http://dx.doi.org/10.1016/j.addma.2017.03.004

This content is provided under CC BY-NC-ND 4.0 license

DIPARTIMENTO DI MECCANICA ■ POLITECNICO DI MILANO
via G. La Masa, 1 ■ 20156 Milano ■ EMAIL (PEC): pecmecc@cert.polimi.it
http://www.mecc.polimi.it
Rev. 0

ACCEPTED MANUSCRIPT

Selective laser melting of pure Zn with high density for biodegradable implant manufacturing

Ali Gökhan Demir[1]*, Lorenzo Monguzzi[1], Barbara Previtali[1]

[1]Department of Mechanical Engineering, Politecnico di Milano, Via La Masa 1, 20156 Milan, Italy

*Corresponding author; aligokhan.demir@polimi.it

Abstract

Zinc and its alloys constitute the new generation of biodegradable metallic materials for biomedical implants. Biodegradable implants of Zn, customized for the specific patient can be potentially realised through additive manufacturing processes. However, Zn is characterized by low melting and boiling points, resulting in high porosity in the build parts. In this work, the selective laser melting (SLM) of pure Zn powder is studied to improve part density. A flexible prototype SLM system was used to determine process feasibility under different atmospheric conditions. Working in a closed chamber under inert gas was found to be inadequate. Process stability was obtained in an open chamber with an inert gas jet flow over the powder bed. The effect of laser process parameters and powder size was studied in this condition. Part density over 99% was achieved in optimal processing conditions.

Keywords: Zinc; biodegradable metals; selective laser melting; custom implants

1. Introduction

Selective laser melting (SLM) has proven to be a powerful tool for biomedical implant manufacturing, especially for the industrial production of customized orthopaedic and dental implants [1]. SLM also provides the use of lattice structures, controlled and interconnected porosity and fine microstructure, which

ACCEPTED MANUSCRIPT

are all potentially beneficial for tailoring the properties of the biomedical implant. Both research communities and industry have been studying the process on established biomedical implant materials, namely stainless steel [3-5], Cr-Co [6-9] and Ti-alloys [10-15]. More recently, biodegradable metals have gained attention for applications concerning temporary grafting. By using a biodegradable implant, ~~a~~ second surgery for implant removal can be avoided in the case of a growing infant patient [16]. Different Mg and Fe based biodegradable alloys were studied, with degradation and biological behaviour being the main issues. Mg is highly suitable as an element because abundantly present in the human body, but Mg implants degrade too rapidly [17]. On the contrary, the degradation rate of Fe is too slow and its alloying elements can be toxic [18]. A newer family of biodegradable metals based on Zn has emerged in recent years. In terms of degradation rate, Zn stands between Mg and Fe. From this point of view, the use of Zn and its alloys is highly promising for smaller implants such as cardiovascular stents and dental implants. Their use in larger implants, however, should be better investigated due to the toxicity risk caused by an excessive level of Zn intake [19-20]. The use of SLM on Zn parts can also benefit the regulation of part density, geometry and microstructure, which are all important factors for regulating the degradation rate and the mechanical properties. Hence, the use of SLM can be considered in order to enhance the properties of implants with standardized geometries such as screws, rods and cardiovascular clips. The processability of Mg and Fe alloys by SLM has been investigated in ~~the~~ recent years [21-27], but there is no detailed literature on Zn and its alloys. This is mainly due to the low processability of this material by SLM and to the rigidity of industrial SLM systems in processing new materials. Characterized by low melting and vaporization points and a limited gap between the two, the SLM of Zn can be instable and give a low part density. In order to benefit from the SLM enabled features on biodegradable Zn alloys, the process should be stabilized to achieve high density.

In SLM, porosity is commonly attributed to the used energy density (fluence) level. Both insufficient and excessive energy densities can cause porosity due to lack of fusion in the former case, and melt pool instabilities in the latter [28-29]. Fluence is studied as a function of the main process parameters, namely laser power, scan speed, hatch distance and layer thickness [1]. Depending on the material type, the process feasibility windows for obtaining high density parts can be determined. In order to obtain functional parts with good mechanical properties, the fluence should remain stable during the whole build to maintain the

ACCEPTED MANUSCRIPT

high density. However, the laser beam can be attenuated, diffracted and scattered within the process chamber as the process fumes and particles build up. Zinc has low melting and vaporization temperatures [30], which can be limiting factors for undergoing SLM. The small interval between melting and vaporization temperatures implies a small fluence range for process stability, whereas a low vaporization temperature may induce excessive smoke and particle build-up during the process.

This work investigates the SLM of pure Zn for biodegradable applications with the aim of identifying processability conditions. In particular, a prototype SLM system was employed to explore different processing atmospheres. Water atomized powder, both as received and sieved, was compared for processability under different fluence levels. The effect of the particle size suspended in the process atmosphere on laser beam scattering is discussed, in addition to the effect of fluence level on particle size.

2. Materials and methods

2.1. Material

Water-atomized pure Zn powder was used throughout the experiments (Metalpolveri, Brescia, Italy). The powder was produced by water atomization, which consists in the impingement of a falling stream of molten metal with a jet of water that rapidly solidifies the metal in small grains. The powder purity was 99.7% as declared by the producer. An energy-dispersive X-ray spectroscopy (EDS) analysis revealed an oxygen content of 2.7 ±0.9 wt%, expected to be inherent from the water atomization process. It should be noted that the EDS measurements are indicative of the surface oxidation due to the sensing depth. The powder was characterized by an irregular shape (see Figure 1.a). In order to test the effects of powder granulometry, coarse and fine particle sizes were used. For the coarse condition, the powder was used in its as received condition, whereas the powder was sieved with a 43 μm mesh (Figure 1.b) to obtain the fine granulometry. The particle size was measured through image processing over SEM images. The image size was 870x590 μm^2. The particle size was evaluated as the average of diameters measured at 2 degree intervals and passing through the particle centroid. Although the particle shape is not globular, this approximation was employed primarily to constitute a comparative basis between the sieved and the as received powders. Size distributions were found to fit a log-normal distribution as depicted in Figure 2. The mean particle size was

ACCEPTED MANUSCRIPT

measured as 15 µm for the coarse powder, and 9 µm for the fine one. Base plates (substrate) were 2 mm-thick cold-rolled plates of pure Zn.

2.2. Selective laser melting (SLM) system

A prototype SLM system developed in-house, namely Powderful, was used throughout the study, allowing flexible control over all the process parameters. A multimode fibre laser source with 1 kW maximum power (IPG Photonics YLR-1000, Cambridge, MA, USA) was connected to a scanner (El.En. Scan Fiber, Florence, Italy). The scan path trajectory was designed using LogoTag software (Taglio, Piobesi D'alba, Italy). The optical chain was composed of a 60 mm collimating lens and a 255 mm f-theta lens. In this configuration, the beam diameter at the focal plane (d_0) was calculated as 212 µm. The main specifications of the laser system are summarized in

. The Powderful system employed a fully automated powder bed and could operate in the controlled processing chamber under process gas or in an open atmosphere with a gas jet flow over the powder bed. The powder deposition system was designed and realized in-house. The control of the system and monitoring of the machine state was carried out in a LabVIEW environment (National Instruments, Austin, TX, USA). In the case of processing in the closed chamber configuration, a vacuum was applied down to 50 mbar of pressure first, and then process gas was introduced. This procedure was repeated 3 times. The system could also be operated in an open chamber configuration with a gas jet parallel to the powder bed surface and suction system on the opposite side of the gas jet.

In the present configuration, the process variables were the laser power (P), the scan speed (v), the hatch distance between the adjacent scan track (h) and layer thickness (t). Throughout the study, the volumetric energy density, fluence (F), was calculated using the following expression:

$$F = \frac{P}{v \cdot h \cdot t} \quad (1)$$

2.3. Characterization

Metallographic cross-sections of SLM parts were prepared by cutting the specimens perpendicular to the

ACCEPTED MANUSCRIPT

scan direction, mounting them in resin and polishing them. Optical microscopy images of the entire specimen cross section (5x5 mm^2) were acquired with a 5X objective lens in order to avoid dependency on the image position (Quick Vision ELF from Mitutoyo, Kawasaki, Japan). The apparent density (ρ_A) was calculated on the images employing image processing software using the following relationship:

$$\rho_A(\%) = \left(1 - \frac{A_{pore,tot}}{A_{tot}}\right) \cdot 100 \quad (2)$$

where $A_{pore,tot}$ is the sum of the pore areas and A_{tot} is the total area examined [31]. The Archimedes method was not applied for the density measurement in order to avoid possible corrosion within the measurement. The biodegradability of the material renders it susceptible to corrosion in water or similar solvents. Sample coatings were avoided for similar reasons. The pore shape was also examined. Measurements over cross-section images have also been proven as accurate in literature for high density conditions [31]. The diameter of the largest pore (D_{max}) was measured for each condition. The average roundness of the found pores (R_{avg}) was calculated from:

$$R_{avg} = \frac{1}{n}\sum_{i=1}^{n} \frac{{P_{pore,i}}^2}{4 \cdot \pi \cdot A_{pore,i}} \quad (3)$$

where P_{pore} and A_{pore} are the perimeter and area of the single pore measured and n is the total number of pores present. The roundness of a perfectly circular shape is equal to 1, with the value increasing as the perfectness deteriorates. All measurements related to pores consider isotropy around the specimens. In order to have a better estimate of the porosity characteristics, all conditions were replicated and a single image of the whole cross-section was acquired instead of sampling in different positions. Vickers microhardness was measured on samples with high density, with a 300 gr applied load (Metkon MH-3, Bursa, Turkey). Fifteen measurements were made along the axis of the build direction, which were used to calculate the average and standard deviation values. An energy-dispersive X-ray spectroscopy (EDS, Inca Energy 200 from Oxford Instruments, Abingdon, United Kingdom) was used within a scanning electron microscope (SEM, EVO-50 from Carl Zeiss, Oberkochen, Germany). EDS was applied to SLM produced specimens with density over 98%, initial powder and the substrate material for comparative purposes. For each condition, five measurements were taken at distinct positions in an area of 870x590 μm^2 at a sensing depth of up to 5 μm.

ACCEPTED MANUSCRIPT

2.4. Experimental plan

The experimental phase was conducted in two distinct stages. In the initial stage, process stability was sought through the study of the processing atmosphere. Due to its low melting (T_m=693 K) and vaporization (T_v=1180 K) points [30], Zn proves to be a difficult material for processing through SLM. The processability of Zn can be compared to AISI 316L (T_v=3273 K), an austenitic steel that is proven to be easily processed by SLM [4,33], by means of a one-dimensional heat flow model to calculate the time required to reach vaporization [32]:

$$t_v = \frac{\pi}{\alpha} \cdot \left(\frac{T_v \cdot k \cdot \pi \cdot d_0^2}{8 \cdot A \cdot P}\right)^2 \quad (3)$$

where α is the heat diffusivity, k is the thermal conductivity, P is the laser power, d_0 is the laser beam diameter, and A is the optical absorption. Zn has higher heat diffusivity (α_{Zn}=43·10^{-6} m^2/s; $\alpha_{AISI\ 316L}$=5·10^{-6} m^2/s), higher heat conductivity (k_{Zn}=113 W/m·K; $k_{AISI\ 316L}$=20 W/m·K) and higher absorptivity at a 1 μm wavelength (A_{Zn}=55%; A_{Fe}=35%) [34,35]. Hence, Zn evaporation is expected to start in a time scale which is approximately 5 times shorter than what is required for AISI 316L. Excessive vaporization and particle ejection during SLM can generate deterioration in part quality, due to fast contamination of the processing chamber. An atmosphere contaminated by metallic vapour and particles affects the transmissivity of the laser beam and optical elements such as the protective window of the scan head. Such deterioration can manifest in a slow manner as the process chamber is contaminated by the build-up of large components, which require long processing times. Preliminary experiments, however, showed that processing Zn in a closed atmosphere under processing gas results in extremely fast contamination of the processing chamber.

An experimental campaign to identify a processing environment suitable for Zn was conducted. The effect of working in a closed and an open process chamber was tested. The effect of process gas was also included, as the process was applied under Ar and N_2 in the closed chamber, and under Ar, N_2 gas jets with a 20 Nl/min flow rate and in ambient air in the open process chamber. The surface finish of the substrate was also included in the study. The surface finish plays an important role for the first few layers of the process in terms of optical reflectivity, but also the mechanical grip of the coated powder. If the initial layers do not attach well to the build plate, they can be stripped off by the recoater, resulting in the complete failure of the build part. Substrates with a cold rolling finish (as received) and increased roughness manually generated

ACCEPTED MANUSCRIPT

using a 60 mesh abrasive paper (roughened) were tested. All experiments using the coarse powder were carried out with a 50 μm layer thickness (t), and 110 μm hatch distance between adjacent scan lines (h). Fluence was applied at only two levels, 127 J/mm^3 (P=281 W, v=400 mm/s) and 147 J/mm^3 (P=242 W, v=300 mm/s), to assess its interaction with the processing environment. Forty layers were melted to reach a 2 mm deposit height. Each condition was replicated twice. A single substrate held 2 replications of the fluence levels, possessed a determined surface finish and was processed at a given processing atmosphere. The results were analysed qualitatively, assessing the adhesion state of the layers.

In the second phase SLM was applied in a stable processing environment. As determined during the initial phase, all experiments were applied in an open chamber with an Ar jet. In order to improve part density, the effect of fluence and powder type was tested. In order to test the effects of powder compactness and its possible interaction with the powder particle size, the layer thickness (t) was varied at 30 and 50 μm. The hatch distance (h) was varied between 110 and 220 μm. The laser power (P) and scan speed (v) were varied to maintain a similar range of fluence for the different levels of layer thickness. All conditions were replicated twice. Specimens with a 5x5x5 mm^3 volume were produced, adapting the number of layers to the layer thickness. The process parameters are summarized in Table 2. The resultant fluence values varied between 20 and 122 J/mm^3.

3. Results

3.1. Effect of the processing atmosphere on process stability

Figure 3 presents images of the process chamber throughout the SLM process applied in a closed chamber. The visibility through the clear chamber reduces rapidly as the process continues layer by layer. By the end of the 5th layer, the chamber is full of vaporized Zn and ejected particles. In these conditions, process stability was absent and Zn deposits did not adhere to the substrate material.

Figure 4 shows example images of specimens belonging to stable and unstable processing conditions. Under unstable processing, the deposits did not adhere well to the surface, which could be removed manually, and showed a remarkably low height compared to the processed layers (see Figure 4.a). Under stable processing,

ACCEPTED MANUSCRIPT

the deposits successfully adhered to the substrate, despite not being optimized in terms of surface roughness or geometrical integrity (see Figure 4.b).

In Table 3, the results of the process stability study are reported. None of the combinations in the closed process chamber were suitable for complete adhesion of the deposits to the substrate. As observed in the preliminary experiments, the use of different fluence levels did not provide any improvement. In all conditions, the process chamber filled rapidly with Zn vapour and powder. On the other hand, all conditions operating in the open process chamber provided stable process conditions. No apparent effect of the gas type or substrate surface finish was found on the adhesion of the deposits to the substrate. In the light of these results, all consecutive experiments were carried out in an open process chamber under Ar gas jet with roughened substrates.

3.2. Optimization of part density

Figure 5 gives example images of the produced specimens in a wider fluence range for depicting the related issues outside the feasibility region. The influence of fluence is evident from the images, since both low and excessive energy density conditions present themselves in a distinct manner. Adhesion to the substrate could not be achieved at low fluence levels ($F<21$ J/mm^3), with partial deposits being left on the substrate surface (see Figure 5.a). In excessive fluence conditions ($F>115$ J/mm^3), specimen disintegration was observed at the higher number of layers due to explosive behaviour. As a result of heat accumulation, particle ejection occurred in an increasing manner at consecutive layers, resulting in a final burst of material at a higher number of layers (see Figure 5.b).

Figure 6 shows the cross sections of the Zn specimens obtained with SLM in different fluence and powder conditions. Evidently, the increase of fluence improves the porosity up to the excessive fluence limit, causing the explosive behaviour in the high number of layers. Another important factor is related to the powder type used. Porosity appears to be higher with similar fluence levels if fine powder is used. Moreover, pore shape and dimensions vary as the part density increases. The pores with lower fluence levels appear to be larger and non-circular. As the part density improved, the pores become more circular and smaller.

ACCEPTED MANUSCRIPT

Figure 7 reports the apparent density measurements as a function of the processing conditions. It can be seen that the powder granulometry conditions the density levels. High density is only available with the coarse powder (see Figure 7.a). At above 40 J/mm^3 the process achieves a stable trend around the density values above 99% for coarse powder. The process remains stable until 115 J/mm^3, above which complete parts could not be achieved due to the material burst caused by heat accumulation. On the other hand, fine powder could not be processed successfully to obtain fully dense parts. With fine powder, the process became highly instable when above 75 J/mm^3, and no complete part could be obtained (see Figure 7.b)

Figure 8 shows the porosity characteristics of the produced Zn parts. Both maximum pore diameter and average roundness decay as the density increases, confirming the previous observations. With higher density levels, the smallest pores are observed as having a diameter of less than 70 µm for coarse powder, while the roundness values converge towards 1.1 as the density increases. The pores appear to be slightly rounder with fine powder around low density levels (ρ_A<95%). In Figure 9, optical microscopy images of pores in low and high density conditions are presented. In the case of the low density part (Figure 9.a), large pores as large as the layer thickness and pores that propagate between the layers are visible. The insufficient fluence generates non-molten zones that deviate the pore shape from the circular one. Higher energy density provides complete melting and the pores are expected to be generated in the solidification phase (Figure 9.b).

Figure 10 depicts the chemical composition of the powder, built specimens and the cold-rolled build plate (substrate). The chemical composition of the SLM produced Zn samples was 98±1 wt% Zn and 2±1 wt% O, with an oxygen content similar to that of the powder. The measurement is qualitative due also to the difficulty in revealing the O content through EDS analysis, and indicates surface oxide content at a superficial layer. However, it can be deduced that the oxygen content did not increase due to the operating conditions in an open atmosphere with ~~a~~ gas jet. Figure 11 demonstrates the microhardness measurements on SLM produced parts with high density (ρ_A>98%) as a function of fluence. A slight increase in hardness is observed as opposed to the cold-rolled counterpart, whereas no significant difference can be seen between the different fluence conditions. On average, the SLM parts are characterized by a hardness of 42±9 HV, whereas that of the cold-rolled pure Zn is 34±2 HV.

ACCEPTED MANUSCRIPT

4. Discussion

In order to assess the limitations in the processability of pure Zn, different aspects should be examined. The first point to be considered is the physical properties of the processed material. Literature on SLM of low melting point materials in general and of Zn in particular is scarce. However, the laser welding of Zn-plated steels has been studied extensively in literature [36-40]. Porosity formation in laser welding has mainly been linked to the entrapment of Zn vapour in the keyhole. Gas entrapment within the melt pool can occur also during the SLM process due to the high amount of vapour generation.

Zn vapour generated in the process can be detrimental to the process in other manners. The vapour pressure can eject material from the melt pool as well as the powder near the molten pool. While operating in a closed chamber, a high amount of vapour and particulate obscure the propagating laser beam in the successive layers because of Rayleigh and/or Mie scattering [32]. Accordingly, the laser fluence is reduced due to absorbed laser power, and the beam shape changes as a result of scattering. The saturation of the processing environment is linked to the time required to settle a particle in equilibrium conditions. In an SLM process, a higher settle time means a higher amount of particle accumulation in the build atmosphere. Two main forces, namely drag force and gravity, act on a particle determining its settle time. Drag force (F_D) acting on a spherical particle can be expressed as

$$F_D = \frac{3 \cdot \eta \cdot \pi \cdot d_p \cdot v_t}{C_c} \tag{4}$$

where η is the fluid viscosity, d_p is the particle dimension, C_c is Cunningham's slip correction factor and v_t is the terminal velocity at which the drag force is balanced with gravitational force [41]. The gravitational force acting on a single particle can be calculated from

$$F_g = \frac{(\rho_p - \rho_f) \cdot \pi \cdot d_p^3 \cdot g}{6} \tag{5}$$

where ρ_p and ρ_f are the particle and fluid densities respectively, and the contribution of ρ_f can be neglected. In equilibrium conditions, the drag and gravitational forces will be equal, hence the terminal velocity can be calculated as:

$$v_t = \frac{C_c \cdot \rho_p \cdot g \cdot d_p^2}{18 \cdot \eta} \tag{6}$$

ACCEPTED MANUSCRIPT

Using Eq.11, a comparative analysis can be carried out as a function of different materials and particle sizes. In particular, Zn can be compared to Fe as the basic element of the ferrous alloys. The settling time can be approximated as the fall time (t_{fall}) of the particle after reaching equilibrium. On average, each particle would travel a distance of 200 mm to deposit on the bottom of the process chamber. For particle dimensions between a diameter of 0.2-20 μm, C_c can be roughly considered constant and estimated as 1, and terminal velocity values can be calculated. Considering that the viscosity of the Ar processing gas is $2.23 \cdot 10^{-5}$ Pa·s, the fall time of Fe and Zn as a function of particle dimension is shown in Figure 12.a. As the graph depicts, the strongest factor that affects the settling time is the particle size, as the sub-micrometric particles remain in the processing atmosphere for much longer. The influence of material density, however, is more limited. This analysis concludes that the main difficulty in processing Zn compared to ferrous alloys is due to the higher amount of smaller generated particulates that hang in the processing atmosphere.

Figure 12.b depicts an agglomerate of deposited particles during the processing of Zn powder. It can be seen that the agglomerate consists of larger particles (>10 μm) and smaller ones (≤1 μm). The morphology of the larger particles is consistent with the powder morphology; hence, these particles are expected to be ejected from the proximity of the process zone due to the pressure gradients caused by the material vapour and the molten phase. The smaller spherical particles are expected to generate from the molten phase that is ejected from the melt pool during the process. The smallest particles, which decrease to nanometric size, are expected to generate from the condensed vapour. This is the portion of deposited agglomerate that remains in the ambient atmosphere for the longest time. According to the calculations, a large Zn particle with a 20 μm diameter deposits in 0.3 seconds, whereas very fine particles with diameters of 200 nm deposit in 8 hours.

The increased amount of particulate generation requires adequate circulation and filtration systems for industrial operations. Conventional SLM systems are equipped with such systems, which are usually dimensioned for operating with alloys that are not prone to excessive vaporization under laser irradiance. From the oxidation point view, Zn is more stable, allowing ~~for~~ operation in an open atmosphere. Providing a larger atmosphere avoids saturation of the processing zone with particulate, and prevents loss of laser irradiance. In practical applications, this implies the use of larger chambers. In the event that more powerful circulation systems are used, the process chamber should be designed to prevent turbulent flows disturbing

ACCEPTED MANUSCRIPT

over the powder bed as well as the process zone. The results showed that the gas jet was also sufficient for protecting the working zone, as demonstrated by the chemical composition measurements. However, for biomedical applications, greater control over the chemical composition, hence the oxide content, is required. Increasing the melting and vaporization points of Zn by increasing the ambient pressure was not taken into consideration because they are not an industrially viable option. In order to increase the melting temperature of Zn by 1 K, a pressure increase of approximately 220 bar is required, whereas to increase the vaporization temperature of Zn to the melting point of steel (approximately 1640 K), the pressure increase should be 26 bar [42,43].

The sensitivity of Zn to laser irradiation is also present under stable operating conditions without ~~the~~ saturation of the processing environment with particulate. The study shows that fully dense parts are acquired in a given fluence range (F=40-115 J/mm^3) by coarse powder that is characterized by large size distribution of between 5-100 µm. Above the stability region, Zn tends to burst and the part disintegrates. This type of instability is different compared to the decay in part density as observed in other metals with a higher melting temperature. Fine powder, on the other hand, proves to be much more sensitive to fluence levels. Spierings et al. demonstrated that with finer powder the energy density required to obtain fully dense stainless steel parts decreased compared to the case when larger powder size was used [44,45]. Larger particle sizes have been demonstrated to increase the optical penetration depth and reduce beam attenuation, which can reduce the melting efficiency [46]. It can therefore be deduced that sensitivity to the vaporization of Zn powder increases as the particle size decreases for the same amount of volumetric energy density.

Other important points for process stability are powder morphology and chemistry. Water atomized powder can influence pore formation. Water atomized powders have been reported to produce porosity due to their high gas content. Li et al. [47] reported that a high oxygen content can reduce ~~the~~ wettability and cause the balling phenomenon, which increases ~~the~~ porosity. Such pores are large in size (>100 µm). The irregular shape of the powder can also inhibit good flowability and generate an irregular powder bed [48]. Neither the balling phenomenon, nor powder bed irregularities were observed within the work. On the other hand, both the oxygen content of the powder and the process gas can become entrapped in smaller fractions within the melt pool, resulting in the formation of small round pores [49,50]. The porosity formation observed is

ACCEPTED MANUSCRIPT

expected to be mainly due to lack of fusion at low fluence and small fractions of entrapped gas within the melt pool at optimal fluence levels.

The pure Zn parts with high density obtained from SLM show a slight increase in microhardness. For single phase materials, an increase in the hardness compared to cast and wrought counterparts is due to the fast cooling cycles in SLM [51,52], which generate finer microstructures. Mostead *et al*. showed that the use of Mg and Al in Zn binary alloys increases microhardness and parallel mechanical properties because of grain refinement and generation of a secondary phase in the alloy [53]. The results of this study depict the microhardness of SLM produced parts to be at an intermediate zone between cold worked pure Zn and extruded Zn-0.15Mg alloy.

5. Conclusions

This work demonstrates the SLM of pure Zn for future applications of biodegradable implant manufacturing. In particular, the processing strategies to obtain fully dense parts were demonstrated for this material with a low vaporization point. Operating in a closed processing chamber resulted in the immediate saturation of the atmosphere, resulting in laser beam scattering and incomplete fusion. The low vaporization temperature of pure Zn results in excessive vapour formation and material ejection from the process zone. The small particulates hang in the process chamber for prolonged periods before settling. Operating under a gas jet with an open process chamber avoided this defect. In stable processing conditions, it was observed that the processability window consisted of incomplete fusion in low fluence values (<40 J/mm^3) and high density in moderate (40-115 J/mm^3) values for coarse powder. At higher fluences (>115 J/mm^3), the process was stable for a few layers, after which the parts disintegrated with a burst of previously deposited layers from the built part. Finer powder was also demonstrated to be more sensitive to fluence variations, since fully dense parts were more difficult to obtain. Pore shape also varied as the part density increased. Large non-circular pores were observed with low density, confirming the lack of fusion in and between consecutive layers. As the density increased, however, the pores became smaller and rounder. Parts with a density higher than 99% could be obtained in stable operating conditions. The parts with high density (ρ_A>98%) were further analysed for chemical composition and microhardness. The oxidation level was similar to that of the powder at 2 wt%.

ACCEPTED MANUSCRIPT

On average, the microhardness was 42 HV, slightly higher than the pure Zn counterpart, due to the high cooling rates within the SLM process.

The implications of the present work on biodegradable device manufacturing using pure Zn and its alloys are multiple. The process chamber should maintain a clean atmosphere, otherwise working with an open chamber can be considered, to avoid saturation of the atmosphere. As a consequence, modifications on existing systems regarding process gas handling may be required. The use of different beam shapes, for instance a flat-top profile, can be beneficial for providing ~~a~~ more homogenous heating over the material. Different processing strategies for distributing the energy on this heat sensitive material can also improve ~~the~~ process stability. Process monitoring for defect recognition or avoidance of catastrophic effects such as part collapse is another important aspect. On the biological side, the behaviour of the SLM produced material *in-vivo* and *in-vitro* should be assessed. As demonstrated by the initial assessment of the mechanical properties, their degradation and mechanical behaviour in the biological environment can be expected to be different due to the employed manufacturing path.

Acknowledgements

The authors wish to express their gratitude to Eligio Grossi, Francesco Mora and Matteo Bonacina for their contribution to prototype development. El.En and Taglio are acknowledged for their technical support. Ehsan Mostaed is acknowledged for his help with the substrate preparation.

ACCEPTED MANUSCRIPT

References

1. D. D. Gu, W. Meiners, K. Wissenbach, R. and Poprawe, "Laser additive manufacturing of metallic components: materials, processes and mechanisms," Int. Mater. Rev., vol. 57, no. 3, pp. 133–164, 2012
2. H. Meier and C. Haberland, "Experimental studies on selective laser melting of metallic parts," Materwiss. Werksttech., vol. 39, no. 9, pp. 665–670, 2008
3. E. Yasa and J.P. Kruth, "Microstructural investigation of selective laser melting 316L stainless steel parts exposed to laser re-melting," Procedia Eng., vol. 19, pp. 389–395, 2011
4. C. Kamath, B. El-Dasher, G.F. Gallegos, W.E. King, and A. Sisto. "Density of additively-manufactured, 316L SS parts using laser powder-bed fusion at powers up to 400 W," Int. J. Adv. Manuf. Technol., vol. 74, no. 1-4 pp. 65–78, 2014.
5. L. E Murr, S.M. Gaytan, D.A. Ramirez, E. Martinez, J. Hernandez, K.N. Amato, P.W. Shindo, F.R. Medina, and R.B. Wicker, "Metal Fabrication by Additive Manufacturing Using Laser and Electron Beam Melting Technologies," *J. Mater. Sci. Technol.*, vol. 28, no. 1, pp. 1–14, 2012
6. X.Z. Xin, N. Xiang, J. Chen, and B. Wei. "In vitro biocompatibility of Co-Cr alloy fabricated by selective laser melting or traditional casting techniques," Mater. Lett., vol. 88, pp. 101–103, 2012
7. X.Z. Xin, N. Xiang, J. Chen, and B. Wei. "Surface Properties and Corrosion Behavior of Co-Cr Alloy Fabricated with Selective Laser Melting Technique," Cell Biochem. Biophys., vol. 67, no. 3, pp. 983–990, 2013
8. C. Song, Y. Yang, Y. Wang, D. Wang, and J. Yu. "Research on rapid manufacturing of CoCrMo alloy femoral component based on selective laser melting," Int. J. Adv. Manuf. Technol., vol. 75, no. 1–4, pp. 445–453, 2014.
9. B. Vandenbroucke and J.P. Kruth. "Selective laser melting of biocompatible metals for rapid manufacturing of medical parts," Rapid Prototyp. J., vol. 13, no. 4, pp. 196–203, 2007
10. R. Stamp, P. Fox, W. O'neill, E. Jones, and C. Sutcliffe. "The development of a scanning strategy for the manufacture of porous biomaterials by selective laser melting," J. Mater. Sci. Mater. Med., vol. 20, no. 9, pp. 1839–1848, 2009

ACCEPTED MANUSCRIPT

11. S. Amin Yavari, R. Wauthle, J. Van Der Stok, a. C. Riemslag, M. Janssen, M. Mulier, J. P. Kruth, J. Schrooten, H. Weinans, and a. a. Zadpoor, "Fatigue behavior of porous biomaterials manufactured using selective laser melting," *Mater. Sci. Eng. C*, vol. 33, no. 8, pp. 4849–4858, 2013.

12. S. Zhang, Q. Wei, L. Cheng, S. Li, and Y. Shi, "Effects of scan line spacing on pore characteristics and mechanical properties of porous Ti6Al4V implants fabricated by selective laser melting," *Mater. Des.*, vol. 63, pp. 185–193, 2014.

13. B. Song, S. Dong, B. Zhang, H. Liao, and C. Coddet, "Effects of processing parameters on microstructure and mechanical property of selective laser melted Ti6Al4V," *Mater. Des.*, vol. 35, pp. 120–125, 2012.

14. H. Attar, M. Calin, L. C. Zhang, S. Scudino, and J. Eckert, "Manufacture by selective laser melting and mechanical behavior of commercially pure titanium," *Mater. Sci. Eng. A*, vol. 593, pp. 170–177, 2014

15. H. Gong, K. Rafi, H. Gu, T. Starr, and B. Stucker, "Analysis of defect generation in Ti-6Al-4V parts made using powder bed fusion additive manufacturing processes," *Addit. Manuf.*, vol. 1, pp. 87–98, 2014.

16. Y. F. Zheng, X. N. Gu, and F. Witte, "Biodegradable metals," *Mater. Sci. Eng. R Reports*, vol. 77, pp. 1–34, 2014.

17. F. Witte, N. Hort, C. Vogt, S. Cohen, K. U. Kainer, R. Willumeit, and F. Feyerabend, "Degradable biomaterials based on magnesium corrosion," *Curr. Opin. Solid State Mater. Sci.*, vol. 12, no. 5–6, pp. 63–72, 2008.

18. H. Hermawan, A. Purnama, D. Dube, J. Couet, and D. Mantovani, "Fe-Mn alloys for metallic biodegradable stents: Degradation and cell viability studies," *Acta Biomater.*, vol. 6, no. 5, pp. 1852–1860, 2010.

19. P. K. Bowen, J. Drelich, J. Goldman. "Zinc exhibits ideal physiological corrosion behavior for bioabsorbable stents." *Adv. Mater.*, vol. 25, no. 18, pp. 2577-2582, 2013

ACCEPTED MANUSCRIPT

20. E. Shearier, P.K. Bowen, W. He, A. Drelich, J. Drelich, J. Goldman, and F. Zhao. "In Vitro Cytotoxicity, Adhesion, and Proliferation of Human Vascular Cells Exposed to Zinc" *ACS Biomater. Sci. Eng.*, vol. 2, no., pp. 634-642, 2016

21. C. C. Ng, M. Savalani, and H. C. Man, "Fabrication of magnesium using selective laser melting technique," *Rapid Prototyp. J.*, vol. 17, no. 6, pp. 479–490, 2011.

22. C. C. Ng, M. M. Savalani, M. L. Lau, and H. C. Man, "Microstructure and mechanical properties of selective laser melted magnesium," *Appl. Surf. Sci.*, vol. 257, no. 17, pp. 7447–7454, 2011.

23. K. Wei, M. Gao, Z. Wang, and X. Zeng, "Effect of energy input on formability, microstructure and mechanical properties of selective laser melted AZ91D magnesium alloy," *Mater. Sci. Eng. A*, vol. 611, pp. 212–222, 2014.

24. B. Zhang, H. Liao, and C. Coddet, "Effects of processing parameters on properties of selective laser melting Mg–9%Al powder mixture," *Mater. Des.*, vol. 34, pp. 753–758, 2012.

25. J. P. Kruth, L. Froyen, J. Van Vaerenbergh, P. Mercelis, M. Rombouts, and B. Lauwers, "Selective laser melting of iron-based powder," *J. Mater. Process. Technol.*, vol. 149, no. 1–3, pp. 616–622, 2004.

26. B. Song, S. Dong, S. Deng, H. Liao, C. Coddet. "Microstructure and tensile properties of iron parts fabricated by selective laser melting," *Opt. Laser Tech.*, vol.56, pp. 451–460, 2014

27. B. Song, S. Dong, S. Deng, H. Liao, C. Coddet. "Vacuum heat treatment of iron parts produced by selective laser melting: Microstructure, residual stress and tensile behavior," *Mater. Design*, vol. 54 pp. 727–733, 2014

28. C. Qiu, C. Panwisawas, M. Ward, H. C. Basoalto, J. W. Brooks, and M. M. Attallah, "On the role of melt flow into the surface structure and porosity development during selective laser melting," *Acta Mater.*, vol. 96, pp. 72–79, 2015.

29. C. Panwisawas, C. L. Qiu, Y. Sovani, J. W. Brooks, M. M. Attallah, and H. C. Basoalto, "On the role of thermal fluid dynamics into the evolution of porosity during selective laser melting," *Scr. Mater.*, vol. 105, pp. 14–17, 2015.

ACCEPTED MANUSCRIPT

30. Properties of Pure Metals, “Properties and Selection: Nonferrous Alloys and Special-Purpose Materials”, *ASM Handbook*, Vol 2, ASM International, 1990

31. A.B. Spierings, M. Schneider, and R. Eggenberger. "Comparison of density measurement techniques for additive manufactured metallic parts." *Rapid Prototyp. J.*, vol. 17, no. 5, pp. 380-386, 2011

32. W. Steen and J. Mazumder. *Laser material processing*, 4th edn, Springer, London, 2010

33. C. Yan, L. Hao, A. Hussein, P. Young, and D. Raymont, “Advanced lightweight 316L stainless steel cellular lattice structures fabricated via selective laser melting,” *Mater. Des.*, vol. 55, pp. 533–541, 2014.

34. R. G. Yarovaya, I. N. Shklyarevskii, and A. F. A. EI-Shazly, “Temperature dependence of the optical properties of the energy spectrum of zinc,” *Zh. Eksp. Teor. Fiz.*, pp. 331–334, 1973.

35. Hügel H., Dausinger F., ”Interaction phenomena” in Handbook of the Euro- Laser Academy, Vol. 2, First Edition, 1998

36. R. Fabbro, F. Coste, D. Goebels, and M. Kielwasser, “Study of CW Nd-YAG laser welding of Zn-coated steel sheets,” *J. Phys. D. Appl. Phys.*, vol. 39, no. 2, pp. 401–409, 2006.

37. X. Li, S. Lawson, Y. Zhou, and F. Goodwin, “Novel technique for laser lap welding of zinc coated sheet steels,” *J. Laser Appl.*, vol. 19, no. 4, pp. 259, 2007.

38. D. Colombo, B. M. Colosimo, and B. Previtali, “Comparison of methods for data analysis in the remote monitoring of remote laser welding,” *Opt. Lasers Eng.*, vol. 51, no. 1, pp. 34–46, 2013.

39. D. Colombo and B. Previtali, “Laser dimpling and remote welding of zinc-coated steels for automotive applications,” *Int. J. Adv. Manuf. Technol.*, vol. 72, no. 5–8, pp. 653–663, 2014.

40. A. F. H. Kaplan, M. Mizutani, S. Katayama, and A. Matsunawa, “Unbounded keyhole collapse and bubble formation during pulsed laser interaction with liquid zinc,” *J. Phys. D. Appl. Phys.*, vol. 35, no. 11, pp. 1218–1228, 2002.

ACCEPTED MANUSCRIPT

41. R.C. Flagan and J.H. Seinfeld. Fundamentals of air pollution engineering. Prentice-Hall, Inc., Englewood Cliffs, New Jersey, 1988

42. E.H. Baker. The boiling-point relations of cadmium and zinc at elevated pressures. *Journal of Applied Chemistry*, *16*(11), pp.321-324, 1966

43. J. F. Cannon, "Behavior of the Elements at High Pressures," *J*. *Phys*. *Chem*. *Ref*. *Data*, vol. 3, no. 3, pp. 781–824, 1974.

44. A. B. Spierings and G. Levy, "Comparison of density of stainless steel 316L parts produced with selective laser melting using different powder grades," in *Proc*. *of Solid Freeform Fabrication Symposium*, 2009, pp. 342–353.

45. A. B. Spierings, N. Herres, and G. Levy. "Influence of the particle size distribution on surface quality and mechanical properties in AM steel parts." *Rapid Prototyping Journal* vol. 17, no. 3, 195-202, 2011.

46. R.W. McVey, R. M. Melnychuk, J. A. Todd, and R. P. Martukanitz. "Absorption of laser irradiation in a porous powder layer." *Journal of Laser Applications* vol. 19, no. 4, pp. 214-224, 2007

47. R. Li, Y. Shi, Z. Wang, L. Wang, J. Liu, W. Jiang, "Densification behavior of gas and water atomized 316L stainless steel powder during selective laser melting," *Appl*. *Surf*. *Sci*., vol. 256, pp. 4350–4356, 2010.

48. R. Engeli, T. Etter, S. Hövel, K. Wegener, "Processability of different IN738LC powder batches by selective laser melting," *J*. *Mater*. *Process*. *Technol*., vol. 229, pp. 484–491, 2016

49. G. Kasperovich, J. Haubrich, J. Gussone, and G. Requena, "Correlation between porosity and processing parameters in TiAl6V4 produced by selective laser melting," *Mater*. *Des*., vol. 105, pp. 160–170, 2016.

50. N. T. Aboulkhair, N. M. Everitt, I. Ashcroft, and C. Tuck, "Reducing porosity in AlSi10Mg parts processed by selective laser melting," *Addit*. *Manuf*., vol. 1, pp. 77–86, 2014.

ACCEPTED MANUSCRIPT

51. I. Tolosa, F. Garciandía, F. Zubiri, F. Zapirain, and A. Esnaola, "Study of mechanical properties of AISI 316 stainless steel processed by 'selective laser melting', following different manufacturing strategies," *Int. J. Adv. Manuf. Technol.*, vol. 51, no. 5–8, pp. 639–647, 2010.

52. J. A. Cherry, H. M. Davies, S. Mehmood, N. P. Lavery, S. G. R. Brown, and J. Sienz, "Investigation into the effect of process parameters on microstructural and physical properties of 316L stainless steel parts by selective laser melting," *Int. J. Adv. Manuf. Technol.*, vol. 76, no. 5–8, pp. 869–879, 2014.

53. E. Mostaed, M. Sikora-Jasinska, A. Mostaed, S. Loffredo, A. G. Demir, B. Previtali, D. Mantovani, R. Beanland, and M. Vedani, "Novel Zn-based alloys for biodegradable stent applications: Design, development and in vitro degradation," *J. Mech. Behav. Biomed. Mater.*, vol. 60, pp. 581–602, Jul. 2016.

ACCEPTED MANUSCRIPT

List of figures

List of tables

ACCEPTED MANUSCRIPT

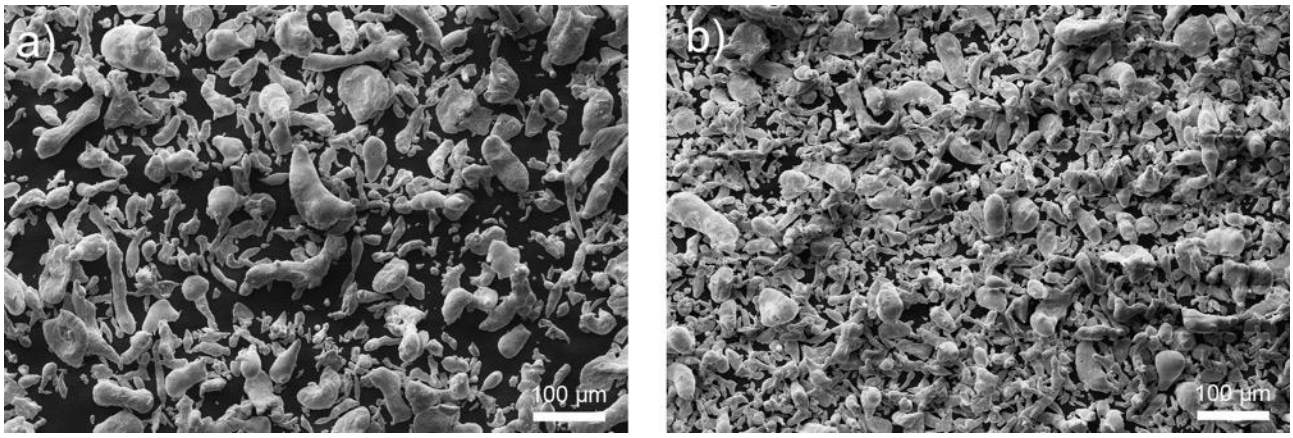

Figure 1. SEM images of the pure Zn powder. a) Coarse and b) fine powder.

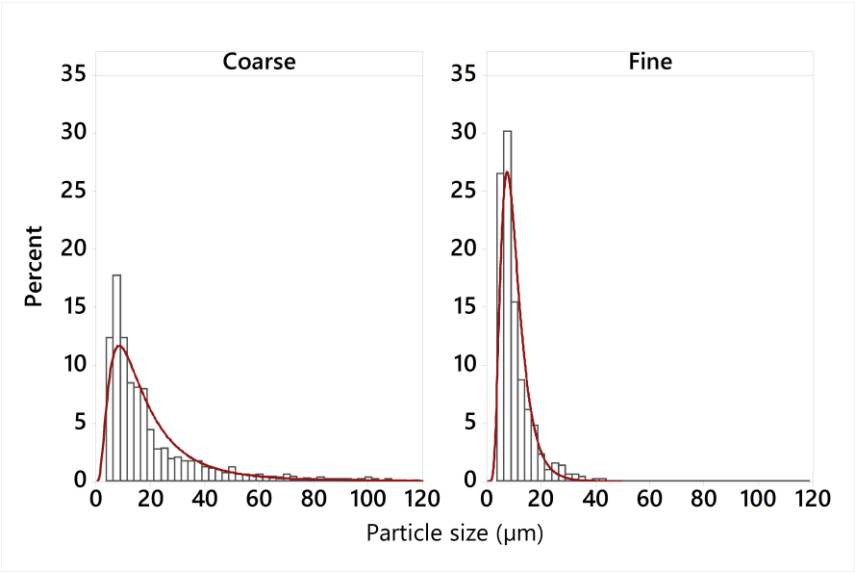

Figure 2. Comparison of the pure Zn powder size distributions in coarse and fine conditions.

ACCEPTED MANUSCRIPT

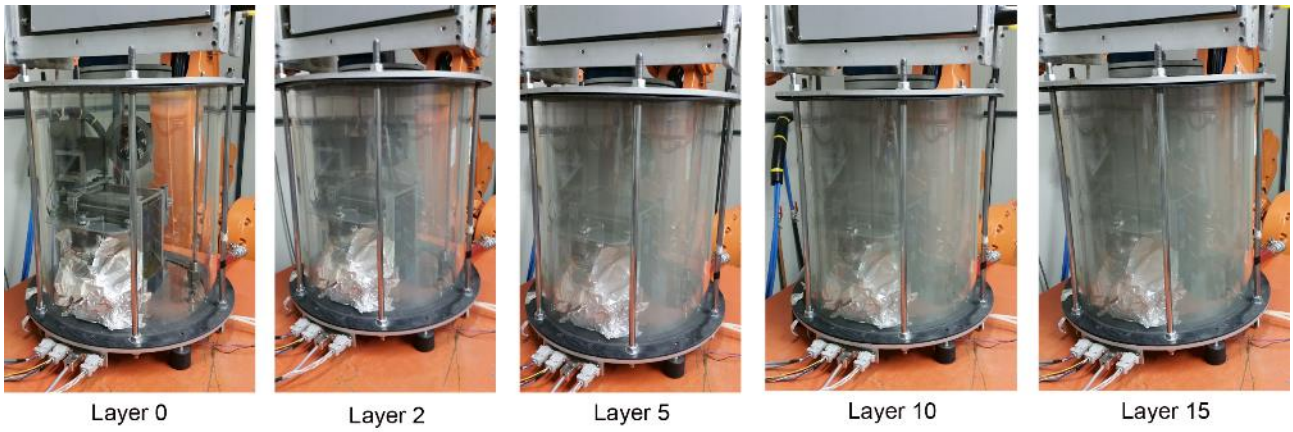

Figure 3. Accumulation of Zn vapour and particles in the processing chamber as the processed layer number increases

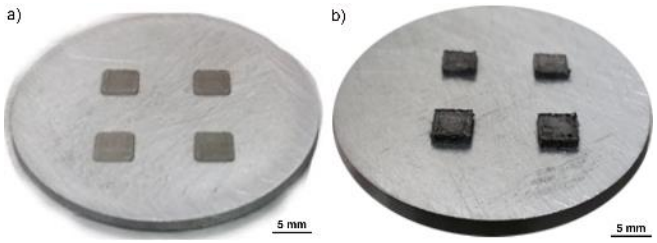

Figure 4. Example images of deposits obtained in the process stability study. a) Specimens showing absence of correct adhesion to the substrate, since only the first layer was found to adhere weakly. b) Specimens showing good adhesion to the substrate with correct height.

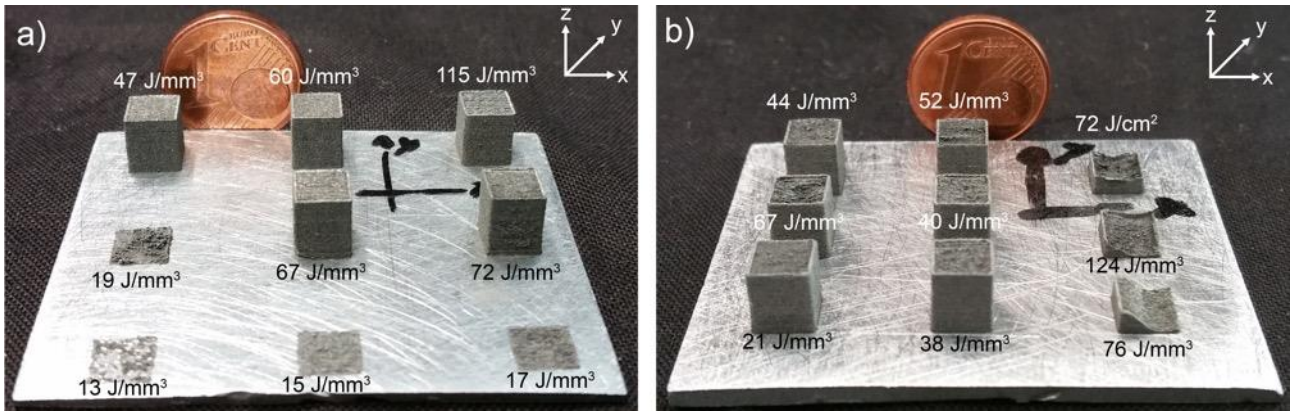

Figure 5. Appearance of SLM produced pure Zn parts showing the effect of fluence. a) Missing parts due to low fluence and incomplete melting with coarse powder, b) missing parts due to excessive fluence and explosive behaviour with fine powder. (x: Scan direction; y: hatch direction; z: build direction).

ACCEPTED MANUSCRIPT

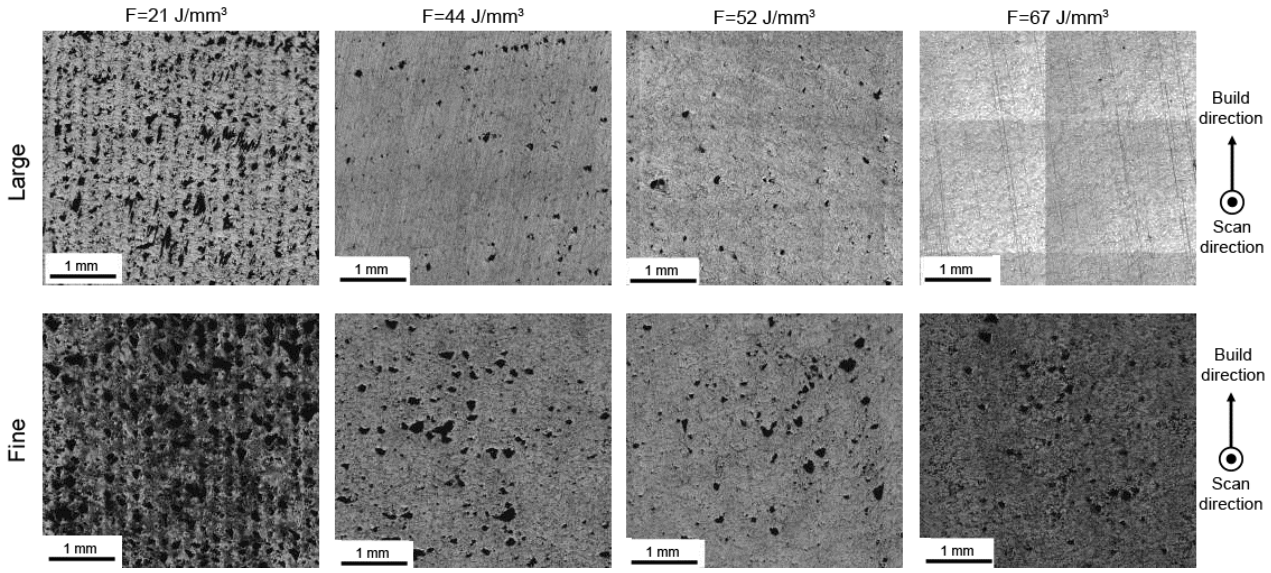

Figure 6. Cross section of the obtained parts, showing the influence of powder type and fluence on material density.

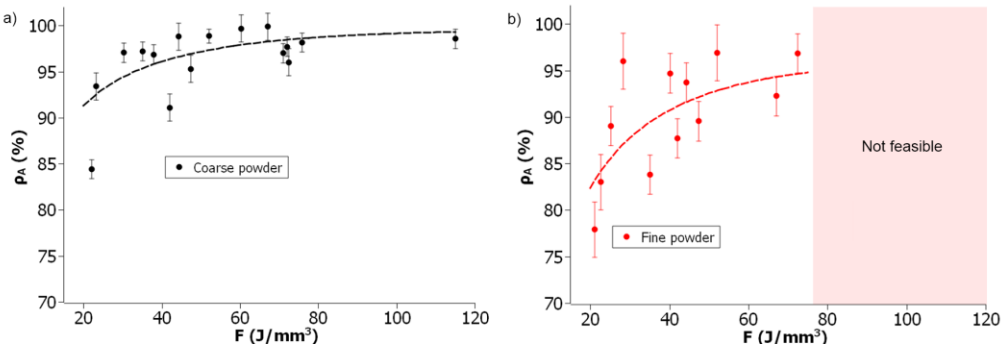

Figure 7. Apparent density values measured over the cross sections as a function of fluence for a) coarse and b) fine powder (error bars represent standard deviation).

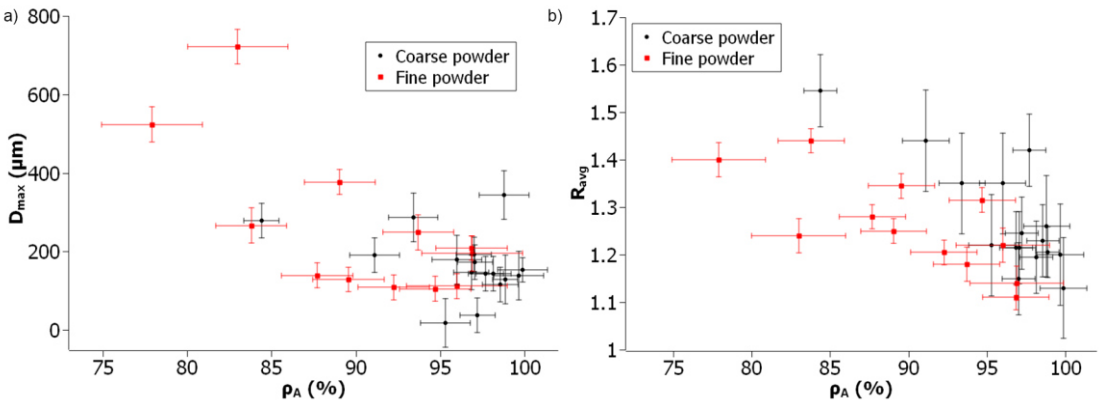

Figure 8. Porosity characteristics of the SLM produced Zn parts. a) Maximum pore diameter measured and b) average roundness of the pores as a function of part density and powder type (error bars represent standard deviation).

ACCEPTED MANUSCRIPT

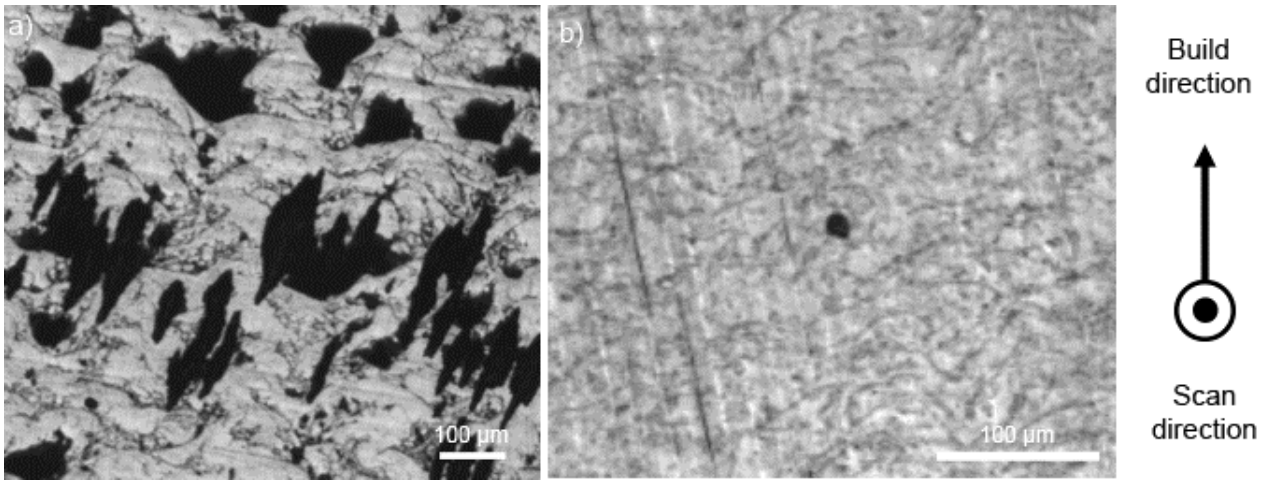

Figure 9. Pore morphology in different part density conditions. a) Incomplete melting with low fluence at F= 21 J/mm^3 showing large pores with a non-circular shape (coarse powder, P=104 W, v=750 mm/s, h=210 μm, t=30 μm), b) complete melting obtained at F=67 J/mm^3 showing a small round pore (coarse powder, P=166 W, v=750 mm/s, h=110 μm, t=30 μm)

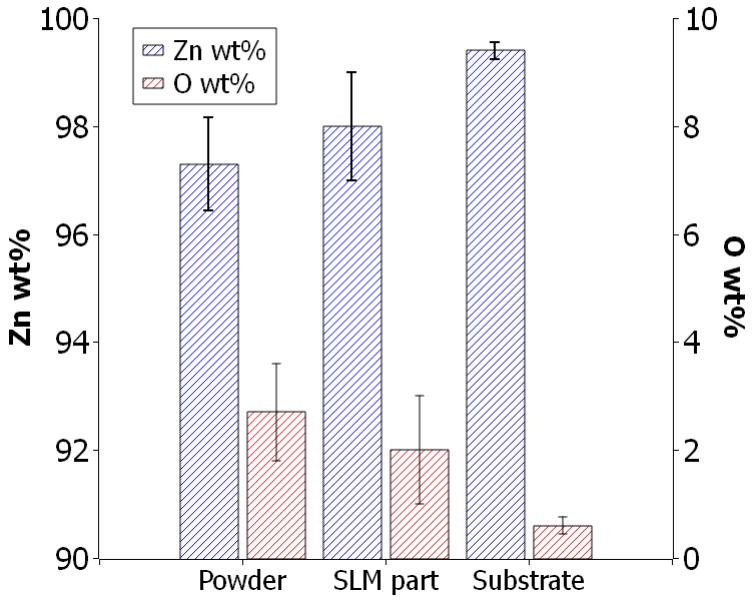

Figure 10. Chemical composition comparison between the initial powder, SLM produced specimens and the build substrate measured by EDS.

ACCEPTED MANUSCRIPT

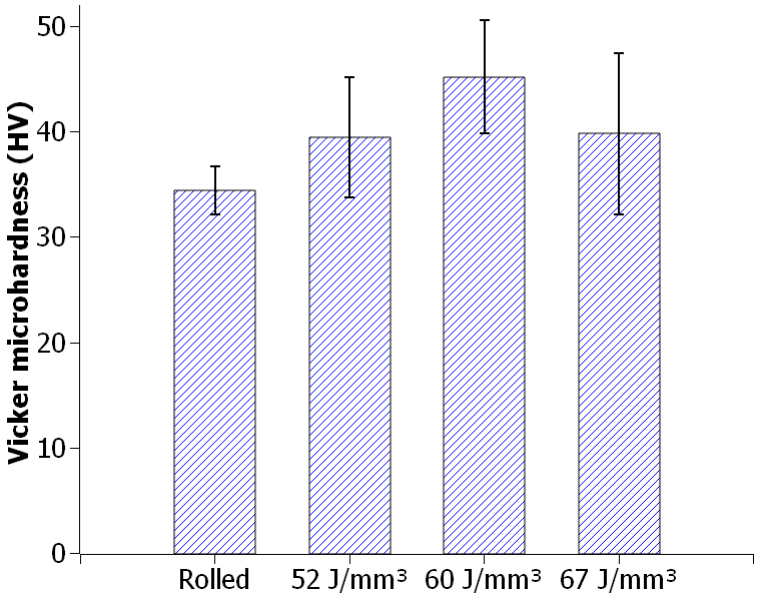

Figure 11. Microhardness of SLM produced Zn parts with high density (ρ_A>98%) compared to the cold-rolled counterpart.

ACCEPTED MANUSCRIPT

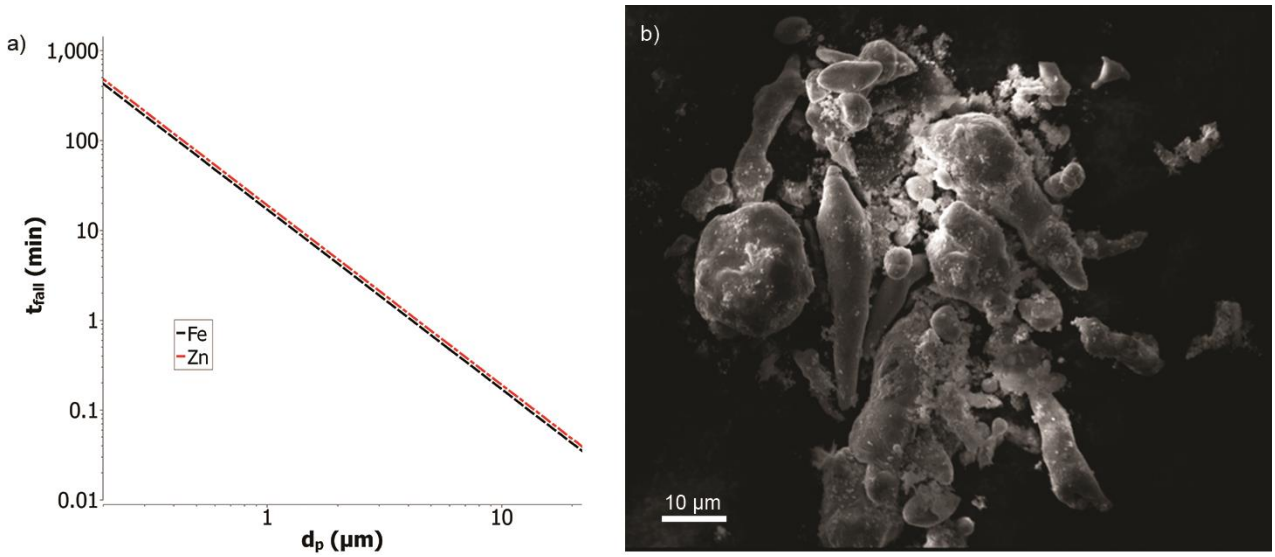

Figure 12. a) Fall time for Fe and Zn as a function of particle dimensions and b) SEM image of Zn particle deposit recovered after process.

Table 1. Main characteristics of the flexible SLM prototype Powderful.

Laser emission wavelength, λ	1070 nm
Max. laser power, P_{max}	1000 W
Beam parameter product, BPP	1.7
Beam quality factor, M^2	5.14
Delivery fiber diameter, d_f	50 µm
Collimation lens, f_c	60 mm
Focal lens, f_f	255 mm
Nominal beam diameter on focal plane,d_0	212 µm
Depth of field, Δz_{pdc}	6.4 mm
Build platform area (DxWxH)	60x60x20 mm^3

Table 2. Fixed and varied parameters in the study of density of Zn parts produced by SLM

Fixed parameters			
Processing atmosphere		Open chamber with Ar jet at 20 Nl/min	
Focal position	Δz (mm)	0	
Varied parameters			
Powder type		Coarse, Fine	
Hatch distance	h (µm)	110-220	
Layer thickness	t (µm)	30	50
Laser power	P (W)	105-166	145-240
Scan speed	v (mm/s)	440-750	350-600

ACCEPTED MANUSCRIPT

Table 3. Results of the experimental study for process stabilization.

Process chamber	Gas type	Surface finish	F (J/mm^3)	Status
Closed	Ar	As received	127	Not adhered
			147	Not adhered
		Roughened	127	Not adhered
			147	Not adhered
	N_2	As received	127	Not adhered
			147	Not adhered
		Roughened	127	Not adhered
			147	Not adhered
Open	Ar	As received	127	Adhered
			147	Adhered
		Roughened	127	Adhered
			147	Adhered
	N_2	As received	127	Adhered
			147	Adhered
		Roughened	127	Adhered
			147	Adhered
	Air	As received	127	Adhered
			147	Adhered
		Roughened	127	Adhered
			147	Adhered